Changes in the hydrological cycle, ocean circulation, and carbon/nutrient cycling during the last interglacial and glacial transition

M. Gröger,[1,2] E. Maier-Reimer,[1] U. Mikolajewicz,[1] G. Schurgers,[1,3] M. Vizcaíno,[1,4] and A. Winguth[1,2,5]

[1] A complex Earth system model has been forced by insolation changes for the last interglacial (LIG) for which geological records evidence a climate cooling that culminated in the last glacial inception. During an early warm period (127–125 ka B.P.) the Arctic/North Atlantic drainage basin north of 30°N receives ~27,000 m^3/s more fresh water mainly imported across the watershed of North America compared to a cooler period centered around 115 ka B.P. Together with a strong surface warming by up to 2 K, this results in a weaker North Atlantic overturning (reduced by ~20%). Sea ice cover is reduced by 3×10^6 km^2 in the Northern Hemisphere, stimulating a stronger productivity in the Barents and Kara seas. In the North Pacific a lowered salinity and a surface warming of more than 3 K increase the stratification. The eastern Pacific becomes nutrient poorer, which leads to a reduction in the export production in areas with vigorous upwelling. The climate cooling in the course of the LIG induces a carbon release by the terrestrial biosphere of 308 Gt, which is counteracted by an oceanic/sedimentary uptake of 290 Gt. The rest remains in the atmosphere increasing the pCO$_2$ by 9 ppm. The large oceanic CO$_2$ uptake corresponds to a rise of the calcite lysocline of about 300 m in the midlatitude Atlantic. The chemically interactive carbonate sediment pool in the Atlantic is reduced by 10%. For nearly the entire North Atlantic, our results are contradictory to the common interpretation of carbonate preservation proxies as a reliable tool for monitoring changes in deep water circulation.

1. Introduction

[2] Triggered by a strong positive summer insolation anomaly, the last interglacial (LIG) between 130 and 115 ka B.P. was the warmest period of the last 250 ka, with summer temperatures up to 4–5°C above present in the Northern Hemisphere [*CAPE Last Interglacial Project Members*, 2006]. Hence the magnitude of the LIG climate warming is comparable to the range that is predicted in the context of future climate warming. The LIG shows a cooling trend which culminated in the inception of the last glaciation. Altogether, a realistic transient climate simulation of the LIG sets an important benchmark for the validation of current climate models.

[3] In this study a fully complex Earth system model with prognostic atmospheric pCO$_2$ is integrated for the first time over 20,000 a of the last interglacial. Insolation forcing at the top of the atmosphere varies between 129 and 109 ka B.P. and is used as the only time varying forcing. This time span corresponds roughly to the Eemian warm period [*Kukla*, 2000]. Previous model studies investigating the effect of insolation conditions corresponding to 125 ka B.P. simulated strong sea surface warming in the Northern Hemisphere [e.g., *Montoya et al.*, 1998; *Kubatzki et al.*, 2000], as well as an intensification of the African-Asian monsoon, caused by higher land-sea temperature contrasts. The importance of snow, ice and biophysical vegetation feedbacks that amplify insolation-forced warming/cooling mainly by modifying the local albedo was emphasized by *Crucifix and Loutre* [2002], *Meissner et al.* [2003], *Kageyama et al.* [2004], and *Schurgers et al.* [2007].

[4] The behavior of the North Atlantic thermohaline circulation (THC) during the LIG is still ambiguous. Both intensified THC [*Kubatzki et al.*, 2000; *Crucifix and Loutre*, 2002] and weakened THC [*Montoya et al.*, 2000; *Wang and Mysak*, 2002; *Khodri et al.*, 2003] have been simulated. Whether the THC was enhanced or not, depended mainly on the poleward atmospheric moisture transport and heat balance. An important influence on the Atlantic freshwater budget is given by the moisture export to the Pacific Ocean via the trade winds and by the import across the Rocky Mountains watershed.

[1]Department of Ocean in the Earthsystem, Max Planck Institute for Meteorology, Hamburg, Germany.

[2]Now at Mainz Academy of Sciences, Humanities, and Literature, IFM-GEOMAR, Kiel, Germany.

[3]Now at Department for Physical Geography and Ecosystems Analysis, Lund University, Lund, Sweden.

[4]Now at Department of Geography, University of California, Berkeley, California, USA.

[5]Department of Earth and Environmental Sciences, University of Texas at Arlington, Arlington, Texas, USA.

[5] Both model studies and pollen based reconstructions especially from high-latitude regions have evidenced a substantial vegetation decline in the course of the LIG [*Kubatzki et al.*, 2000; *Tarasov et al.*, 2005; *Schurgers et al.*, 2006] which points to extensive changes in carbon storage on land. However, from the modeling perspective only few time transient simulations have been performed for past interglacials using models of reduced complexity and focusing on the carbon cycle. *Brovkin et al.* [2002] simulated a decrease of 90 Gt carbon storage on land during the Holocene with the CLIMBER model. By contrast, *Joos et al.* [2004] simulated only slight changes in terrestrial carbon storage throughout the last 8 ka. A problem related to this is associated with the negative climate feedback of carbon released by the terrestrial biosphere which is assumed to herald and accompany the major continental glaciations preserved in geological archives. Since the ice core records of atmospheric pCO_2 indicate rather a decline toward the end of the LIG [*Petit et al.*, 1999], there must have been a substantial oceanic uptake compensating for the terrestrial release of carbon.

[6] Previous studies applied either complex atmosphere-ocean general circulation models (AOGCMs) for equilibrium experiments or more comprehensive Earth system models but with a drastically reduced complexity for time transient simulations. This means that either the time transient behavior is neglected, or feedback mechanisms between individual Earth system compartments that become important especially in time transient changes cannot be modeled in a realistic way as this is possible when using three-dimensional (3-D) GCMs. Therefore, in this study for the first time a 3-D AOGCM providing realistic physics is coupled to a terrestrial biosphere and a 3-D carbon and nutrient cycle model. The latter two compartments encompass a completely closed carbon cycle and allow for a full prognostic simulation of atmospheric pCO_2. The hydrological cycle and atmosphere-ocean-sea ice dynamics are explicitly resolved. The model is used to investigate the following questions:

[7] 1. How does the hydrological cycle change with regard to atmospheric interbasin moisture transports?

[8] 2. How may the thermohaline circulation have changed in response to these alterations of freshwater fluxes?

[9] 3. Can the ocean neutralize changes in terrestrial carbon storage and what are the governing mechanisms?

2. Model and Forcing

2.1. Earth System Model

[10] The Max Planck Institute for Meteorology and University of Wisconsin-Madison Earth System Model (MPI/UW ESM [*Mikolajewicz et al.*, 2007]) is used for this study. The model version applied here consists of the coupled AOGCM ECHAM3/LSG2, a dynamic global vegetation model (LPJ-DGVM [*Sitch et al.*, 2003]) and the marine biogeochemistry model HAMOCC3 [*Maier-Reimer*, 1993]. The latter two components encompass the complete carbon cycle permitting the prognostic simulation of the atmospheric pCO_2 which, in turn, is used for the radiation calculations in the atmosphere model. The ocean is forced with heat,

momentum and freshwater fluxes from the atmosphere which uses sea surface temperature (SST) and sea ice conditions as lower boundary condition. The hydrological cycle is closed by a simple runoff scheme (following the topography gradient) implemented in the ocean model. Continental ice sheets are prescribed according to preindustrial conditions.

[11] The spectral atmosphere model ECHAM3.6 [*Roeckner et al.*, 1992] has a horizontal resolution of approx. $5.625°$ and 19 layers. Flux corrections for freshwater and wind stress are the only artificial modifications. The oceanic component runs on an 64×64 Arakawa E' grid providing an effective resolution of about $4°$. It has 22 layers that increase in thickness with depth. The thickness of the surface and bottom layer are variable to account for seafloor topography and the spatially and temporarily changing sea level. Prognostic variables are temperature, salinity, sea surface height, velocities, and sea ice thickness. The model includes a simple thermodynamic/dynamic sea ice model.

[12] The HAMMOCC3 marine carbon cycle model uses a time step of 1 month. The tracers are advected with the ocean model with a time step of 5 d. The model receives atmospheric wind fields, shortwave radiation, temperature, salinity, and sea ice fields from the OGCM for the simulation of biogeochemical processes. Export production depends on phosphate concentration, temperature, light, and depth of the mixed layer [*Maier-Reimer*, 1993]. Depending on the newly produced particular organic matter (POC), calcitic and silicic shell material is formed with the latter being the preferred builder when sufficient SiO_2 is available. Silica, carbonate and POC fluxes to the ocean's interior are parameterized using individual exponential penetration depths and are assumed to occur immediately. Dissolution of calcite depends on available calcite and the depth-dependent undersaturation with respect to carbonate ions ($[CO_3^=]$). POC is allowed to remineralize when oxygen exceeds a threshold value. A chemically interactive sediment layer permits the simulation of carbonate and silicate accumulation. More details about the formulation of the model's biogeochemistry are given by *Maier-Reimer* [1993].

[13] Temperature, precipitation, absorbed short-wave radiation, soil water content are used as input variables for the terrestrial dynamical vegetation model LPJ, which physically feeds back to the atmosphere via the land surface (i.e., surface background albedo, vegetation and forest cover, as well as roughness length). Changes in the simulated carbon storage are transferred as CO_2 fluxes to the atmosphere. Details of the coupling are given by *Schurgers et al.* [2007]. A detailed description of the MPI/UW ESM together with an equilibrium simulation for preindustrial conditions is provided by *Mikolajewicz et al.* [2007].

2.2. Experimental Setup and Forcing

[14] The average integration time for investigations requiring 3-D GCMs (like, e.g., Intergovernmental Panel on Climate Change scenarios) is usually of the order of decades to a maximum of few hundred years. The integration time of 20,000 a required in this study is thus extraordinary large. However, because the typical adjustment times of individual climate components are of the same order as their
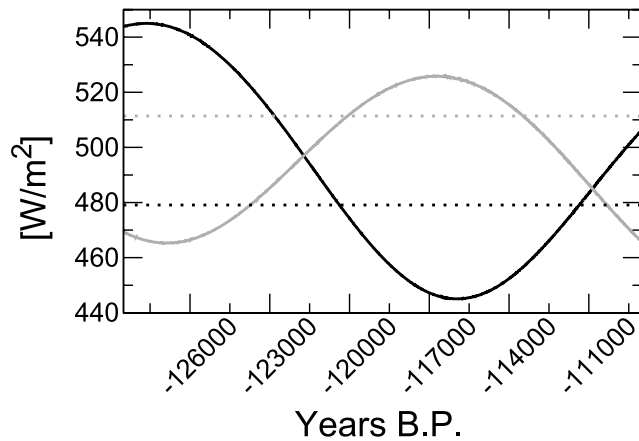
Figure 1. Time evolution of prescribed yearly maximum of daily insolation (W/m^2) at 60°N (black) and 60°S (grey). Values of the control run are indicated by horizontal dotted lines.

characteristic timescales, the highly dynamic model components may only be integrated from time to time. Therefore the simulations presented here were set up using a periodically synchronous coupling scheme [*Voss and Sausen*, 1996] in which the atmospheric module (consuming ~90% of the total integration time) is switched off temporarily. During these asynchronous periods the other model components are driven with archived input data from previous periods in which the atmosphere was integrated online for 24 months (= synchronous periods). The total length of the archive was 8 a. This length was a compromise between the number of years required to give a reasonable representation of both mean and variability of the forcing and between the artificial delay to external forcings, which arise when using forcings being calculated with climate data corresponding to an earlier time. Because of the slow changes in insolation forcing the latter effect is likely to be negligible. The length of the asynchronous periods varied between 8 and 96 a, depending on the amount of changes in atmosphere-ocean heat fluxes. Details of the procedure are described by *Mikolajewicz et al.* [2007]. This coupling technique has been demonstrated to be appropriate for long-term (multidecadal) climate processes as they are addressed in this study and it has been applied for both the ocean components and the terrestrial biosphere. The biogeochemical components are thus not distorted and the timescales of their interaction can be fully exploited. In this configuration the model simulated about 150 a/d on a NEC-SX6. A detailed description of the coupling technique and its validation is given by *Mikolajewicz et al.* [2007].

[15] To spin the model up, it has been integrated for more than 10,000 a with present-day insolation and prognostic atmospheric pCO_2 which finally spread slightly around 279.2 ppm (σ = 3.6 ppm) neglecting anthropogenic changes of the land surface. From this spin-up run an insolation experiment was started in which orbital parameters were forced to change with time using the solution of *Berger* [1978] and a solar constant of 1365 W/m^2.

[16] For slower climate compartments with longer internal timescales it is not feasible to deduce initial fields from an

ideal equilibrium state. Thus the experiment was started from restart files of the spin-up run and the orbital configuration was set to 129 ka B.P. and immediately forced to proceed in time (including interactive dynamic pCO_2). Therefore the first 1000 a could be affected by spin-up effects and are not interpreted in this paper. This insolation run was accompanied by a control run with preindustrial conditions and dynamic calculation of the atmospheric pCO_2 concentration which was started from the same initial fields and integrated for 10,000 a.

[17] Seasonal variations of incoming solar radiation in the course of the LIG were quite large and comprise the evolution from a maximum around 128 ka B.P. to a minimum at 116 ka B.P. for the Northern Hemisphere (Figure 1). The forcing is nearly inverse on the Northern and Southern hemispheres. The major effect is a strengthening (weakening) of seasonal contrasts in the Northern (Southern) Hemisphere. As a result, the yearly maximum insolation was increased by up to 9% compared to the present-day value in the Northern Hemisphere at around 128 ka B.P.

3. Results

3.1. Sea Surface Temperatures

[18] The strong changes in insolation together with amplifying feedbacks related to perennial sea ice cover
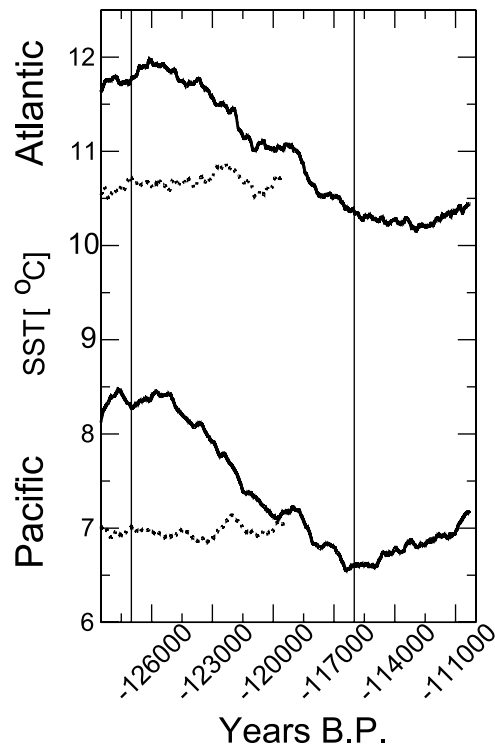

Figure 2. Yearly average sea surface temperature evolution for the Atlantic (top curve) and Pacific (bottom curve) north of 30°N. Dotted curves indicate variability of the control run. Curves are smoothed using a 1000-a running mean. Vertical lines indicate maximum (left) and minimum (right) values for incoming radiation at the top of the atmosphere at 60°N.
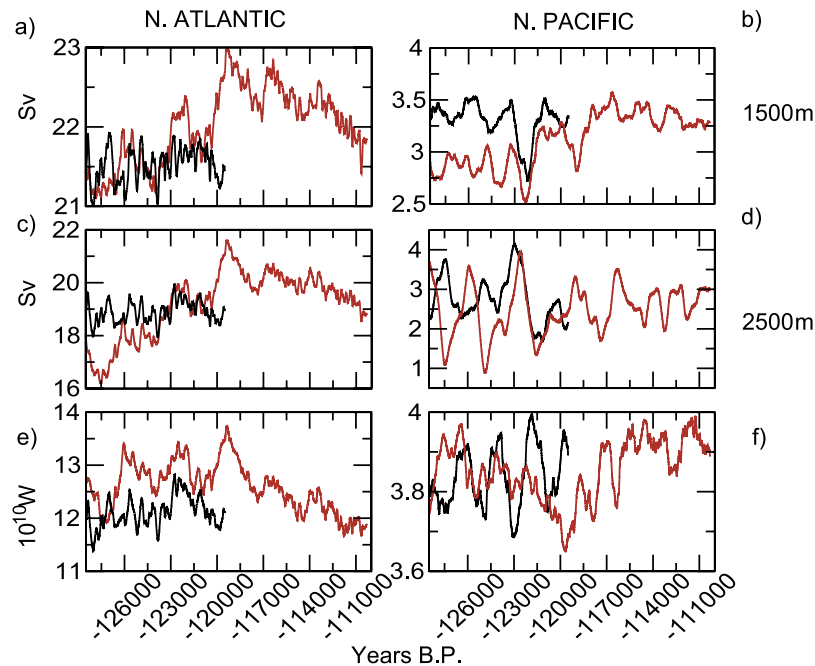
Figure 3. (a) Atlantic overturning (Sv) at 30°N and 1500 m depth. (b) Same as Figure 3a for the Pacific. (c) Atlantic overturning (Sv) at 30°N and 2500 m. (d) Same as Figure 3c for the Pacific. (e) Area-integrated potential energy dissipation due to convection (10^{10} W) in the Atlantic north of 30°N. (f) Same as Figure 3e for the Pacific. Black lines indicate variations of the control run. All time series are smoothed using a 1000-a running mean.

changes (and snow cover on land) result in intense warming of the surface ocean in the Northern Hemisphere. The temporal evolution is characterized by a warm optimum between 127 and 125 ka B.P. followed by a cooling trend (Figure 2). The latest Eemian shows increasing temperatures, which is in agreement with the intensifying insolation.

[19] The inception of the cooling trend lags the insolation maximum by roughly 2000 a in both ocean basins (Figure 2). The 2000-a time span indicates the magnitude rather than the exact timing of the delay as it is impossible to distinguish between stochastic and deterministic signal components which would require a number of ensemble simulations. The magnitude, however, points to a nonlinear response of the annual mean SST to insolation forcing most probably related to the irregular latitudinal distribution of insolation anomalies around the year.

[20] The cooling trend is delayed and smoother in the North Atlantic compared to the North Pacific. This is caused by a rapid strengthening of the Atlantic overturning (Figure 3a) and the northward heat transport counteracting the cooling due to the weakening insolation. Between 40 and 50°N the zonally integrated heat transport (not shown) increases by more than 0.07 PW (15%) from 127 to 119 ka B.P.

[21] A prominent difference is seen also in the timing of the trend reversal in the late Eemian (Figure 2) around 116 ka B.P. The reason for the earlier Pacific reversal is the stepwise establishment of stable convection starting at 119 ka B.P. in the North Pacific (Figure 3f), which forces an increased northward heat transport via the Kuroshio

Stream. In places where the warm and salty Kuroshio merges with the cold waters arriving from the subpolar gyre, convection can reach depths exceeding 1000 m. The northward heat transport between 30 and 40°N increases from 122 to 116 ka B.P. by 10% (0.0325 PW). By contrast, in the North Atlantic the convection shows a stepwise decrease of 12% after 119 ka B.P. until the end of the simulation (Figure 3e). Since the changes in the insolation forcing are extremely small around the insolation extremes, the different evolution of the meridional heat transport has a significant impact on the SST, thus explaining the phase lag in the evolution between the North Pacific and the North Atlantic.

[22] The spatial pattern of sea surface temperature (SST) differences between 126 and 115 ka B.P. is shown in Figure 4a. SSTs in the Northern Hemisphere are increased for 126 ka B.P. compared to 115 ka B.P. by more than 3 K in the NE Pacific and up to 2 K in the North Atlantic. Here, the warming is counteracted by strengthened westerlies carrying cold air masses originating from Greenland and Newfoundland. This occurs primarily during winter when the Icelandic Low is strengthened by up to 7 hPa. In addition, but of minor importance, the northward heat transport is somewhat reduced in the North Atlantic due to the weaker meridional overturning circulation at 126 ka B.P. (Figures 3a and 3c). During the warm optimum the annually averaged area covered by sea ice is shrunk by 3×10^{6} km^2 in the Northern Hemisphere. In regions where the sea ice cover is reduced, the ocean is no longer insulated from the colder atmosphere, and the heat loss to the
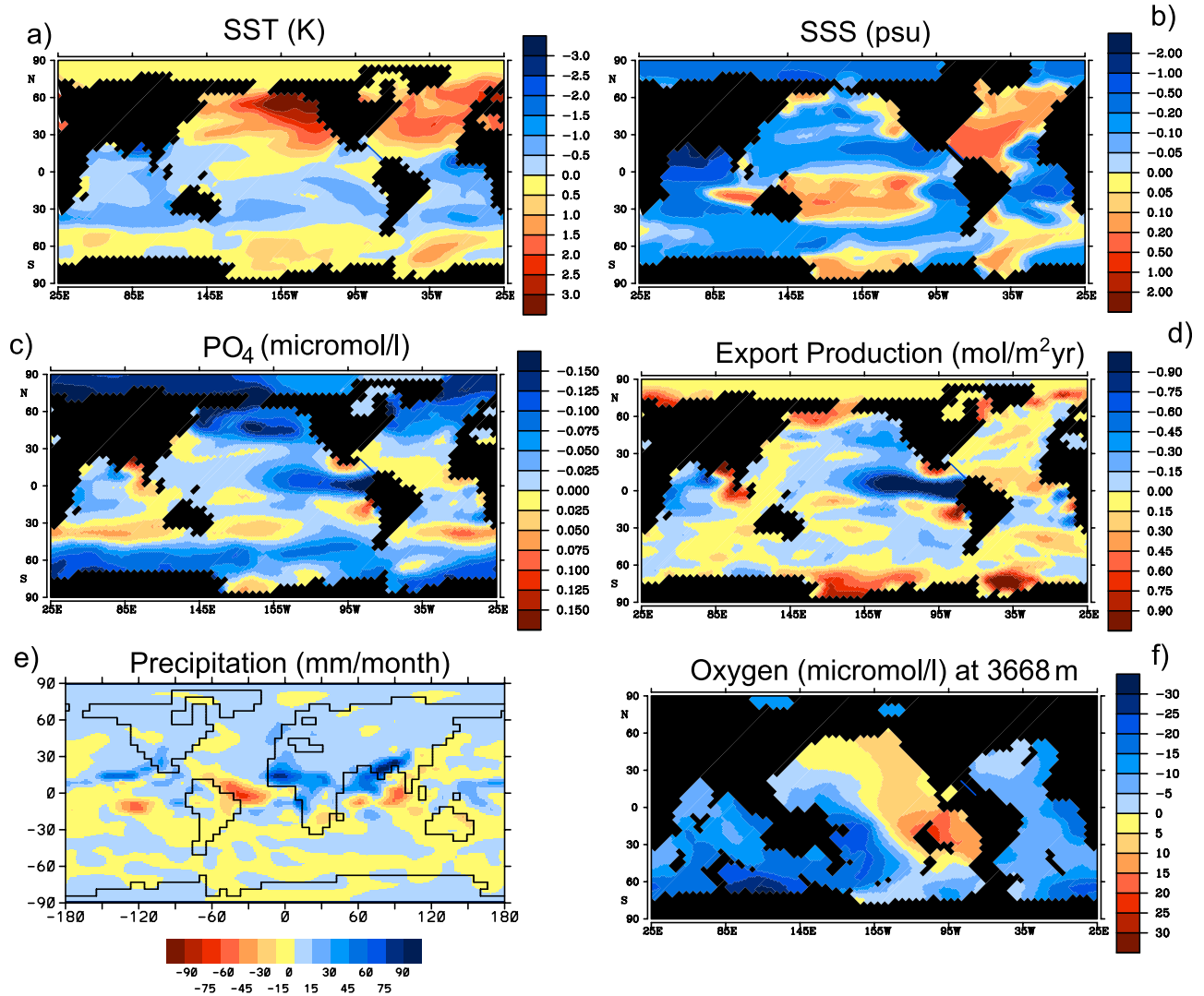
Figure 4. Anomaly (126–115 ka B.P.) for (a) Sea surface temperature, (b) salinity of the second ocean layer (75 m), (c) phosphate at 25 m (μmol/L), (d) export production (mol/m^2 a), (e) precipitation (mm/month), and (f) oxygen concentration (μmol/L) at 3668 m water depth. Anomalies have been derived from 4000-a averages centered around 126 and 115 ka B.P.

atmosphere increases considerably especially during winter, which dampens the surface warming. This effect is largest in the northwestern Pacific and in the entire Arctic.

[23] Cooling is seen in tropical regions due to lower annual mean insolation which is forced by an increased obliquity of the Earth's rotational axis at 126 compared to 115 ka B.P. (Figure 4a). Cooling anomalies for 126 ka B.P. exceeding 1.5 K are simulated for the eastern tropical Atlantic. In this region the cooling is strengthened by changes in heat transport during summer. At 115 ka B.P. trade winds are blowing hot air masses offshore from the extremely heated desert and steppe areas similar to today. At 126 ka B.P. this pattern is disturbed by an anomalous strong monsoon circulation which results in intensified precipitation over NW Africa (Figure 4e). The main wind direction is onshore, and hence there is no westward

advection of hot air masses to the Atlantic. Together with a slightly higher cloudiness at 126 ka B.P. these cooling effects explain the extraordinary large cooling in the eastern tropical Atlantic.

3.2. Hydrological Cycle

[24] In the following we analyze the changes in interbasin freshwater fluxes due to atmospheric moisture transports with emphasis on the Atlantic Ocean. In the long-term mean, the divergence of the vertically integrated horizontal moisture transports is balanced by evaporation and precipitation (neglecting the time rate of change of the vertically integrated atmospheric moisture content):

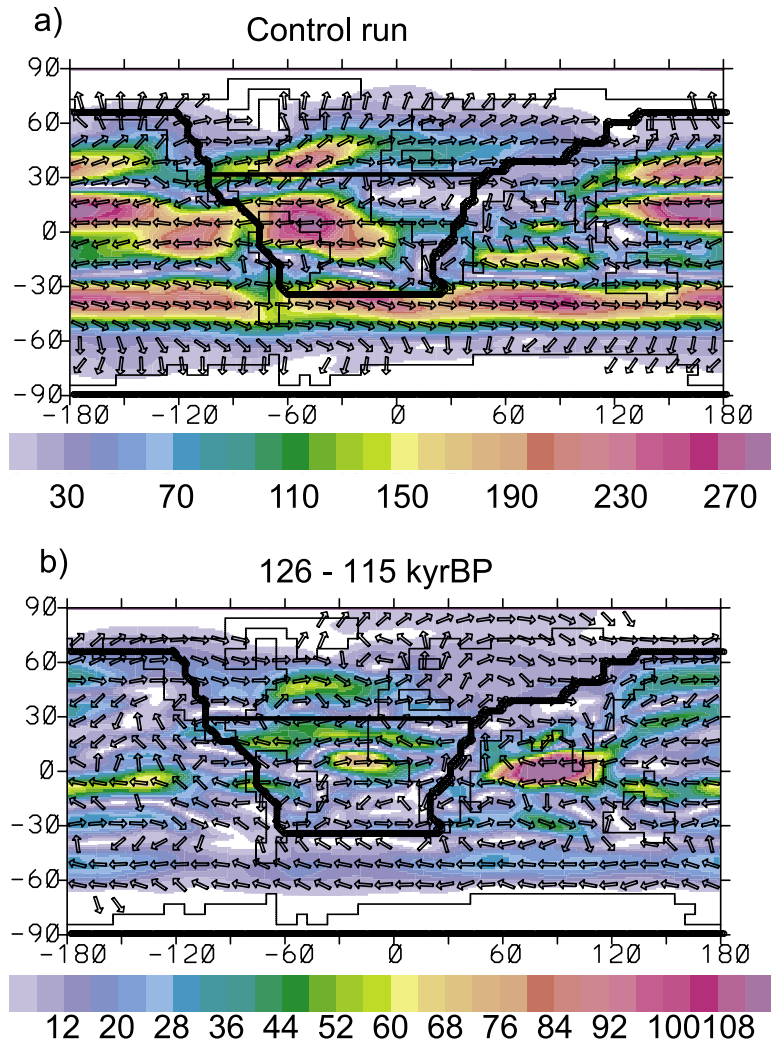$$\nabla \cdot \int_0^p \mathbf{v} q \frac{dp}{g} = E - P \qquad (1)$$

Figure 5. Atmospheric moisture transports (kg/ms) for the (a) control run and (b) 126–115 ka B.P. Black lines indicate the watersheds used to define the Atlantic drainage basin north of 30°S and north of 30°N.

where ∇ denotes the divergence operator, p is the surface pressure, $\mathbf{v}$ is horizontal velocity, q is the water vapor mixing ratio, and g denotes gravity acceleration.

[25] On the basis of a simple runoff scheme in the ocean model, a catchment area for the Atlantic drainage basin has been defined (Figure 5). Both the Atlantic north of 30°S and

north of 30°N are considered separately. For the region north of 30°N the pattern of the control run is at first-order simply enhanced at 126 ka B.P. (Figure 5) compared to 115 ka B.P. The anomalous arrows indicate larger transports over the watersheds of North America and Asia. In total, the North Atlantic receives 27 mSv (1 sverdrup (Sv) =

Table 1. Freshwater Transport Into the Arctic/Atlantic Drainage Basin Across the Watersheds Shown in Figure 5[a]

Period	Total North of 30°N	North America[b]	South Boundary	Asia		
126 ka B.P.	385	269	227	−110		
Control ka B.P.	362 (0.8)	207 (1.0)	233 (1.1)	−78 (0.3)		
115 ka B.P.	358	200	231	−74		

Period	Total North of 30°S	North America[b]	South America	South Boundary	Africa	Asia
126 ka B.P.	−330	379	−402	−322	125	−110
Control	−304 (1.6)	337 (1.3)	−340 (2.0)	−317 (2.3)	95 (1.2)	−78 (0.3)
115 ka B.P.	294	347	−337	−315	86	−74

[a]Parentheses indicate values of the standard deviation derived from the control run. Positive values indicate an import. Transport is in mSv.
[b]Border between the North and South America basin has been drawn at 16.5°N.

10^6 m^3/s) more freshwater (Table 1) at 126 ka B.P. than at 115 ka B.P. Most of the surplus originates from the Pacific and arrives over the Rocky Mountains watershed (+69 mSv). This is partly compensated by larger exports via the Asian watersheds (−36 mSv) into the Pacific whereas the changes along the southern boundary at 30°N are small (−4 mSv). The largest changes are seen in the tropical and subtropical Atlantic (Figure 5b). Whereas the export over Panama is at first order simply enhanced, farther south the transports are affected by substantial changes in the Walker Circulation that lead to a strong east-west dipole pattern in precipitation (Figure 4e) in the tropical Atlantic and surrounding landmasses. During the Northern Hemisphere warm season strong heating over tropical Africa at 126 ka B.P. leads to stronger convection resulting in an anomalous moisture transport from the western and eastern tropical Atlantic to Africa as indicated by the anomalous arrows. In the western tropical Atlantic strong anomalous divergent arrows are seen over Amazonia, where moisture is for the one part exported to Africa at 126 ka B.P. and for the other part a larger volume than at 115 ka B.P. escapes via South America to the tropical Pacific. These changes result in an extremely decreased rainfall in the tropical western Atlantic and a corresponding freshening of the eastern Atlantic which benefits from the increased runoff from the Congo and Niger catchment area (Figures 4e and 4b). In summary, the Atlantic looses freshwater mainly via South America/Panama (65 mSv) and Asia (36 mSv). Only the import over Africa (39 mSv) and from the North Pacific over North America (32 mSv) is enhanced (Table 1). In total, the Atlantic north of 30°S receives 36 mSv less freshwater at 126 ka B.P. compared to 115 ka B.P.

[26] The consequence of these changes is a pronounced dipole pattern seen in the anomalous salinity field (Figure 4b) in the subtropical North Atlantic which extents far into the extratropical Atlantic. The gyre circulation advects saline waters from the western tropical Atlantic via the North Brazil Current, Gulf Stream and North Atlantic Drift far to the north, whereas the freshened waters of the eastern Atlantic are blocked off by the Canary Current in the north. The enhanced moisture transport across the Isthmus of Panama translates into a stronger Pacific-Atlantic salinity gradient around Central America (Figure 4b). Minor positive salinity anomalies near the coasts of South Africa and southern South America reflect a diminished runoff from the Rio de la Plata River and the South African catchment area. This is linked to the weaker monsoon intensity in these regions [*Gröger et al.*, 2007].

[27] Over the open South Pacific a strengthened Hadley circulation during austral winter enhances the subsidence of upper level dry air masses in the subtropics which favors evaporation at 126 ka B.P. and contributes to the increased moisture uptake by the trade winds (Figure 5). This is expressed also in the strengthening of the subtropical high-pressure system by more than 3 hPa (not shown). This explains the moderate and extended positive salinity anomaly in the tropical and subtropical South Pacific (Figure 4b) at 126 ka B.P.

[28] The strong freshening of the Indian Ocean is dominated by the amplified monsoon precipitation. Compared to 115 ka B.P. a larger part of moisture originates from the Pacific via north Thailand/south China. Because of the strengthened monsoon, the Walker Circulation is considerably weakened. This results in lower precipitation over the Gulf of Bengal and enhanced precipitation and decreased evaporation over the Arabian Sea. This pattern resembles the climatic changes which are characteristic for the positive phase of the Indian Ocean Dipole (IOD). It is caused by the relatively strong decrease of SSTs in the eastern Indian Ocean (Figure 4a).

3.3. Impact on Deep Water Circulation
3.3.1. Atlantic

[29] The changes at the ocean surface and atmospheric boundary condition have a significant impact on the Atlantic overturning. The higher surface temperature and salinity at 126 ka B.P. compared to 115 ka B.P. (Figures 4a and 4b) have counteracting effects on density. In case of the Irminger Sea southeast off Greenland, the temperature effect lowers the density up to 0.20 kg/m^3 whereas the higher salinity increases it by maximal 0.1 kg/m^3. The potential energy release due to convection in the Norwegian Sea and northern Irminger Sea is reduced by up to 30% compared to 115 ka B.P. The center of convection moves to the southwest. As a result, North Atlantic Deep Water (NADW) is warmer and saltier.

[30] In the Weddell Sea, deep convection is enhanced for 126 ka B.P. mainly due to a diminished freshwater input of 10 to 20 mm/month which corresponds to a relative reduction of up to 50%. Additionally, sea ice thickness is reduced due to increased convection and increased insolation during austral winter. This increases the heat loss to the atmosphere which feeds back positively on the deep convection. In consequence, the North Atlantic overturning cell is shallowed compared to 115 ka B.P. In the North Atlantic, overturning is reduced by ∼20% (Figure 3a). As a consequence NADW is injected more at intermediate depths to the expense of the deeper layers. The outflow of NADW from the Atlantic at 30°S is reduced below 2500 m by about 3 Sv (20%, not shown). These changes can be monitored in a meridional cross section for salinity along the central Atlantic (Figure 6a). The largest positive anomalies are seen in the North Atlantic. Between 40°S and 40°N a sharp north-south dipole pattern occurs within the upper few hundred meters which reflects the changed surface conditions (Figure 4b) penetrating deepest in the subtropical gyres due to vigorous Ekman pumping. A pronounced feature is the salinity increase between 1000 and 2500 meters which reflects mainly the changed water mass properties of the shallowed NADW in the water column. By contrast, freshening in the deepest layers of the South Atlantic indicates the increased inflow of Antarctic Bottom Water (AABW). A cross section for temperature (not shown) yields an almost identical pattern: strongest warming (up to 0.5 K) at intermediate levels and cooling (up to 0.5 K) in the deep South Atlantic indicating the intensified inflow of AABW.

[31] The Atlantic overturning increases in response to the Northern Hemisphere cooling in the course of Eemian (Figures 1 and 2). An anomalous high maximum is reached
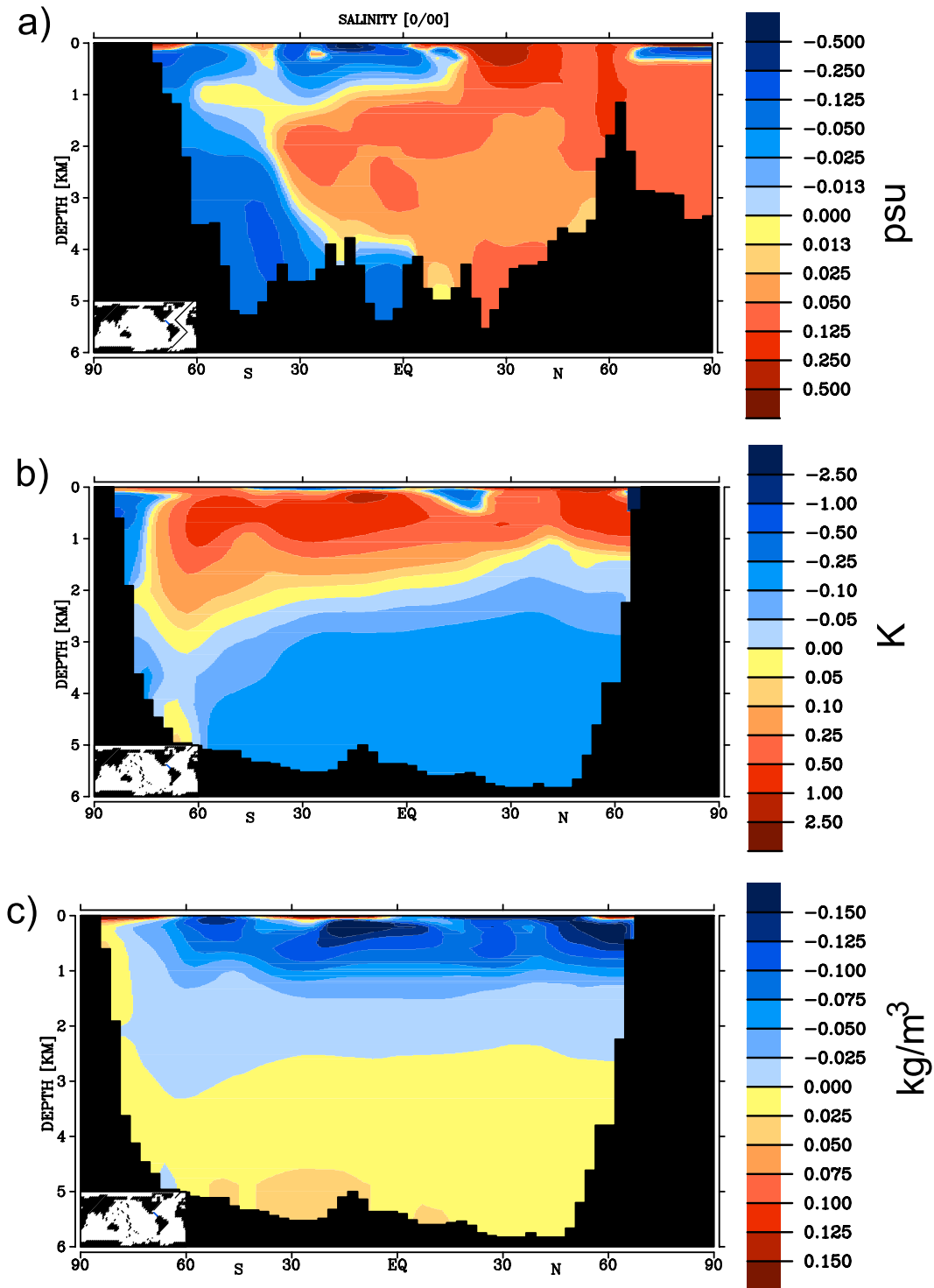
Figure 6. (a) Meridional cross section along the central Atlantic for salinity (difference 126–115 ka B.P.), (b) zonally averaged temperature cross section for the Pacific, and (c) density.

at ∼119 ka B.P. (Figure 3c). The steep increase to this maximum is the result of a combination of three mechanisms.

[32] 1. The peak value falls in a time where the changes ($\Delta Qsw/\Delta t$) in incoming insolation are at their maximum

rate which stimulates accelerated cooling in the northern and maximal warming rates in the Southern Hemisphere (inflection points in Figure 1).

[33] 2. From 119 to 117.5 ka B.P. the deep water production collapses in the Weddell Sea. In this region the energy
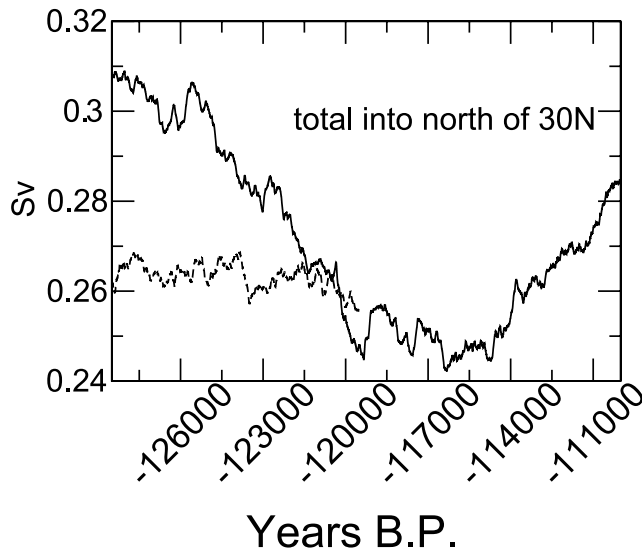
Figure 7. Atmospheric moisture transports into the Atlantic catchment area north of 30°N.

dissipation due to convection decreases by 86%. As a consequence, the inflow of AABW weakens significantly, which strengthens the meridional overturning of NADW especially in the deepest layers.

[34] 3. Finally, the decreasing moisture transports into the North Atlantic culminate in a first minimum between 120 and 119 ka B.P. (Figure 7). Altogether, this leads to the anomalous high overturning around 119 ka B.P.

3.3.2. Pacific

[35] In the upper 2 km the Pacific is warmed by up to 2.5 K in the zonal average (Figure 6b) at 126 ka B.P. compared to 115 ka B.P. Both the lower salinity and the higher temperatures considerably stabilize the stratification in the North Pacific during the early Eemian warm period at 126 ka B.P. (Figures 4a and 4b). The density difference between the surface layer and water masses below 3 km is increased by more than 0.15 kg/m^3 (Figure 6c). This has two consequences: (1) The maximum convection depth in the central North Pacific is reduced by several hundred meters, thereby weakening the production of North Pacific intermediate water; and (2) the stronger stratification weakens the large-scale upwelling of cold deep waters in the North Pacific which is driven by vigorous AABW inflow from the south. As a result of these two changes, the zonally integrated overturning circulation in the North Pacific is weakened in the upper limb where water masses return southward. At 30°N the weakening amounts to about 0.5 Sv (15%) at 1500 m (Figure 3b). However, as the total overturning (depicted at ~2500 m depth) does not change significantly (Figure 3d), the southward return flow is strengthened in the deeper layers mainly along the North American Continental Margin (NACM). The weaker North Pacific upwelling further warms the upper layers, which again increases the stability and feeds back negatively on the overturning. As a result of these changes, the Pacific

surface ocean is considerably decoupled from the deep layers (Figure 6c).

3.4. Changes in Ocean Biogeochemistry and Carbon Cycle

3.4.1. Nutrient Concentrations and Carbon Cycle

[36] During the early Eemian warm period the global export production is slightly reduced (<4%) compared to the colder late Eemian. This reduction arises mainly from the Pacific Ocean while the Atlantic production is slightly enhanced (Figure 4d) for 126 ka B.P. The most pronounced minima are seen in regions with intense or moderate upwelling, e.g., the eastern tropical and the northeastern Pacific.

[37] Nutrient concentration in these areas was substantially reduced as well at 126 ka B.P. (Figure 4c). As the tropical Pacific is nutrient limited today and thus more sensitive to changes in the nutrient supply, the response is stronger than in the North Pacific (although it is more nutrient depleted) where nutrients are only partially consumed [*Takahashi et al.*, 1993]. Although the upwelling intensity is enhanced by 6.5% in the tropics between 90 and 135°W and 10°S and 10°N at 126 ka B.P. compared to 115 ka B.P., the corresponding upward transport of nutrients is reduced by 7.5%. This results from the decoupled surface ocean from abyssal layers (Figure 6c). Likewise, because of the strengthened southward flow of deep waters below 2000 m along the NACM, the deep east Pacific is better ventilated and thus nutrient poorer compared to 115 ka B.P.

[38] These changes in circulation lead to a strong east-west gradient in the anomalous oxygen concentrations in the deep Pacific (Figure 4f). Maximum changes at 126 ka B.P. are simulated around the East Pacific Rise (plus 15% compared to 115 ka B.P.) and around the Ontong Java Plateau (minus 15%). Nearly the same pattern is seen in the nutrient distribution (not shown): Maximum positive anomalies in the southwest and negative anomalies in the east Pacific.

[39] Regions with lower nutrient concentration but increased productivity are found in the high latitudes, e.g., the subpolar western Pacific, the Arctic, and the North and South Atlantic (Figure 4d). These regions benefit mainly from the retreat of sea ice cover and/or from the strong surface warming (Figure 4a). The latter is crucial for calcite precipitating species [*Maier-Reimer*, 1993] which benefit more from the warmer temperatures than opal producers. In the North Atlantic and North Pacific the rain ratio of particular inorganic carbon to particular organic carbon is increased up to 40% for 126 ka B.P. compared to 115 ka B.P. even in regions that are not affected by sea ice. In the North Atlantic the opal production (not shown) is decreased by up to one third for 126 relative to 115 ka B.P. which is caused by the reduced deep mixing and the higher SST which makes carbonate precipitating organisms more competitive. However, due to diminished sea ice cover the opal production extends far into the Arctic at 126 ka B.P. Maximum increases are simulated in the Barents and the Kara seas (Figure 4d), where warm water from the North Atlantic
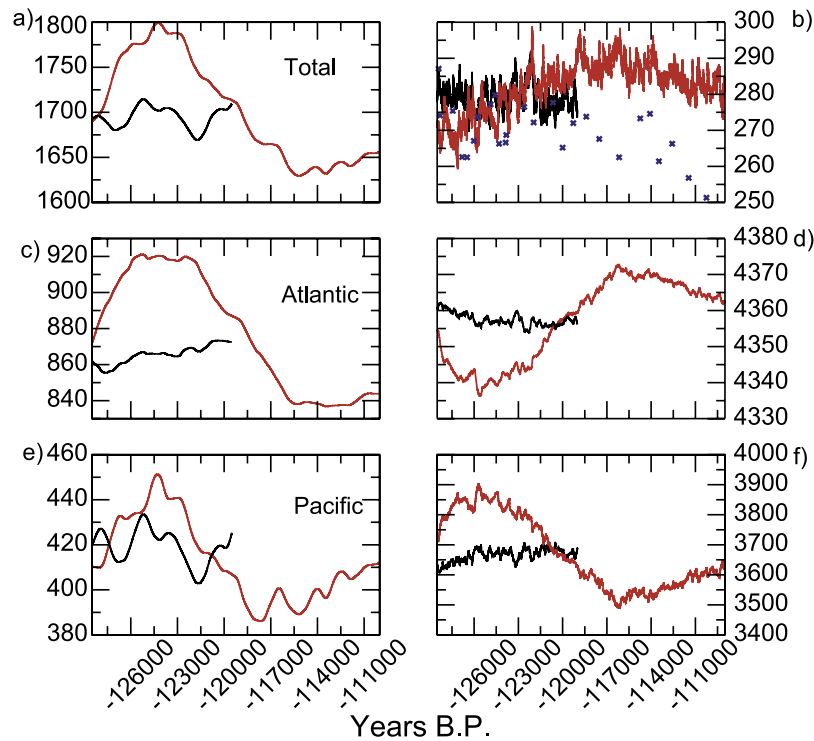
Figure 8. (a) Total, (c) Atlantic, and (e) Pacific sedimentary inorganic carbon (Gt). (b) Atmospheric pCO$_2$ including values from the Vostok record (crosses, from *Petit et al.* [1999]). (d) Total carbon stored in the ocean (Gt). (f) Total carbon storage in the terrestrial biosphere (Gt). Black lines indicate variability of the control run. Displayed are 1000-a running averages except for pCO$_2$.

Drift can penetrate farther north and feed back negatively on sea ice thickness.

[40] A significant increase in export production and nutrient concentration is simulated in the northern tropical Atlantic (Figures 4c and 4d). Between 50.6°W and 2.8°E, the equatorial upwelling is intensified by 3 Sv or 9.5%. This is accompanied by a corresponding increase in upward transport of 2×10^6 μmol phosphate (10%).

3.4.2. Carbon Cycle

[41] The warm climate in the early Eemian causes substantial shifts in the terrestrial vegetation. Northward expanding boreal forests around the Arctic, the greening of the Sahara desert, and a larger vegetation coverage especially in the Northern Hemisphere monsoon belt and in the tropics increase the terrestrial carbon pool by up to 200 Gt in the first 3000 a (a detailed discussion of land carbon storage dynamics is given by *Schurgers et al.* [2006]).

[42] However, the ongoing climate cooling in the course of the Eemian decreases the carbon storage on land again by 308 Gt C from 126 to 115 ka B.P. (Figure 8f). The majority of this loss is linked to the southward retreat of boreal forests and a diminished vegetation in the African tropics and the African-Asian monsoon belt. Increasing carbon stocks were simulated only in the midlatitudes due to a weakened respiration of soil carbon (Figure 9a) associated with cooler temperatures. Although the decrease on land is only about 8% of the total pool (Figure 8f), a corresponding atmospheric uptake would increase the atmospheric pCO$_2$

by about 152 ppm (assuming no further CO$_2$ limitation for plant growth and no exchange with the ocean pool). The simulated change for atmospheric pCO$_2$ remains, however, over most of the experiment below the noise level of the control run (Figure 8b) because the majority of the land carbon release is compensated by oceanic uptake (Figure 8d).

[43] The largest oceanic carbon pool, the total dissolved CO$_2$ (ΣCO$_2$) in the water column (only the chemical active uppermost 10 cm of the seafloor are considered from the sedimentary carbonate), plays by far the most important role in compensating the perturbation arising from the terrestrial biosphere. It increases by ~430 Gt from 126 to 115 ka B.P. An accompanying decrease of 140 Gt is simulated in the carbonate sediment pool (Figure 8a) which is caused by dissolution. This means that about one third of the 430 Gt ΣCO$_2$ increase is balanced by the sedimentary carbonate buffer: The ongoing uptake of CO$_2$ makes the ocean more acidic which reduces the carbonate ion concentration [CO$_3^=$]. This process enhances the carbonate dissolution and hence increases the alkalinity at the ocean surface which, in turn, favors the oceanic uptake of airborne CO$_2$. Only 18.5 Gt of the total release remain in the atmosphere and increase the pCO$_2$ by only 9 ppm on average in the course of the LIG (Figure 8b). Changes in POC (−3.8) sedimentary C$_{org}$ (+3.3 Gt) and calcitic shell material in the water column (−0.3 Gt) are negligible.

[44] Although the relative reduction of the carbonate sediment pool is almost the same for the Pacific (10.0%; Figure 8e) and the Atlantic (8.3%; Figure 8c) the latter
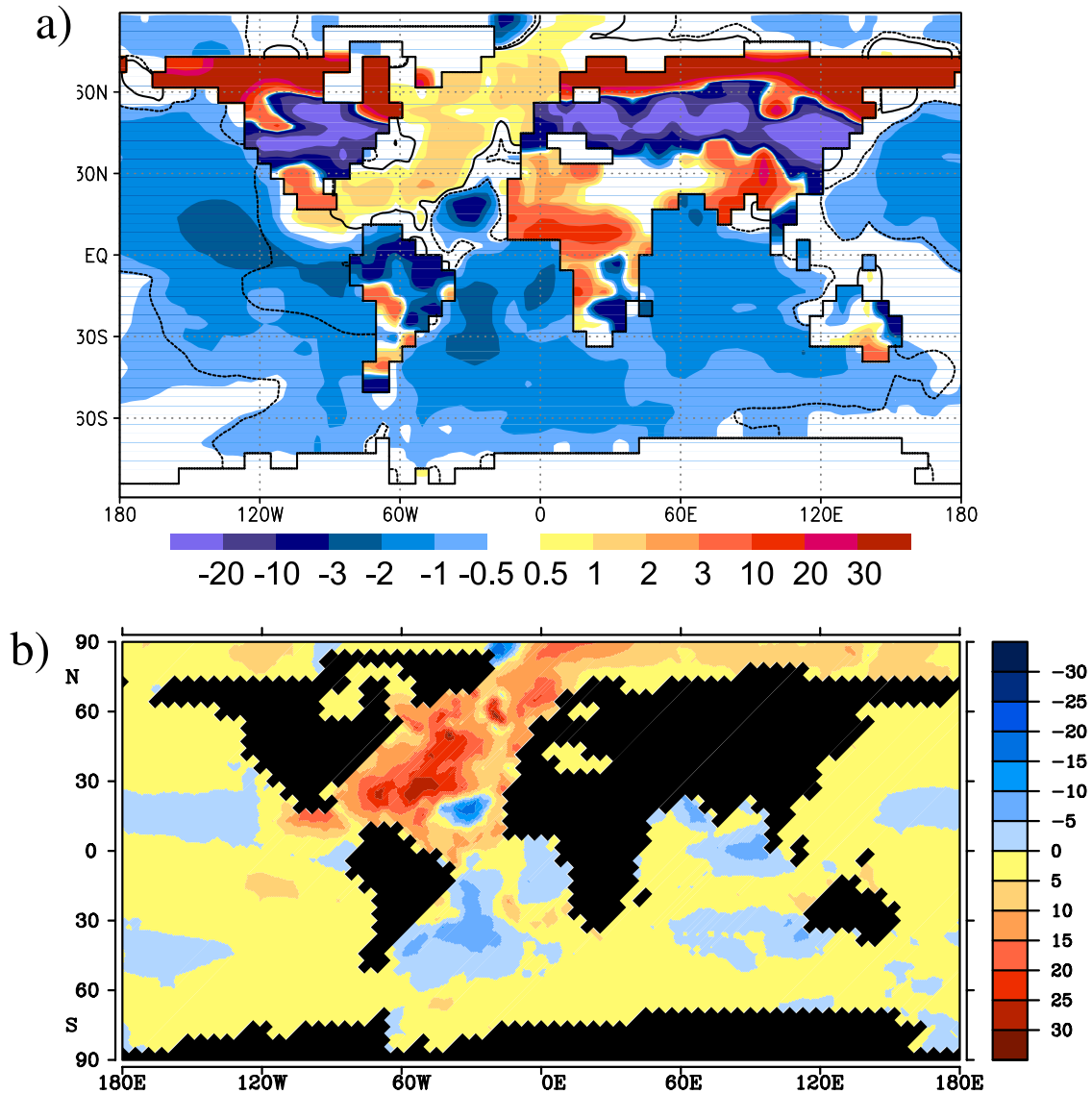
Figure 9. (a) Difference in carbon storage (kg/m^2) between 126 and 115 ka B.P. Black lines indicate the 95% confidence level for the ocean realm. (b) Same as Figure 9a for carbonate sediment (kg C/m^2). The 2000-a averages are shown. Note that reddish colors indicate major sources for atmospheric CO_2 in the course of the Eemian, whereas bluish colors indicate major sinks.

provides, due to its larger pool, the by far most important ocean reservoir considering the carbonate system. From 126 to 115 ka B.P. more than one half (76 Gt) of the 140 Gt reduction of the global carbonate pool is related to the Atlantic. It is followed by the Pacific which, because of its large extension, accounts for at least one third (44 Gt). Only minor contributions come from the Indic (8.9% or 12.5 Gt) and the Southern Ocean (5.5% or 7.9 Gt).

3.4.3. Spatial Pattern of Carbon Uptake and Carbonate Dissolution

[45] Most ocean areas (including sediment pool) exhibit significant carbon accumulation in the course of the Eemian (Figure 9a).This pattern is mainly controlled by the changes in ΣCO_2 (not shown), which gains carbon from the atmo-sphere above and from dissolving carbonate sediments beneath.

[46] The dissolution of the carbonate sediment is strongest in the North Atlantic (Figure 9b) where it leads to a decrease in the total carbon storage (Figure 9a) at 115 ka B.P. compared to 126 ka B.P. In this region the sedimentary carbonate buffer operates very quickly due to the intense deep mixing in the northern North Atlantic associated with deep water production. Additionally, the production of calcitic shell material decreases due to the surface water cooling. The saturation state with respect to carbonate ions (not shown) lowers in the course of the Eemian at all water depths except in the South Atlantic and South Pacific. In the midlatitude northern Atlantic the lowering saturation corre-sponds to a rise of the calcite lysocline of about 300 m.

Increasing carbonate pools are seen in the western South Atlantic and eastern equatorial Atlantic (Figure 9b) where the weaker inflow of corrosive AABW favors carbonate preservation at 115 ka B.P.

4. Discussion

4.1. Thermohaline Circulation

[47] Owing to the complex, meridional and interbasin changes in the atmospheric freshwater transports the model simulates relative large changes in the THC. The evolution of the North Atlantic overturning, namely, the increase by 20% from the warm optimum to its maximum at 119 ka B.P. is followed by the weakening toward the end of the simulation (Figures 3a and 3c). This evolution is in contrast to the more linear and lower amplitude response seen in less comprehensive models. Using an Earth system Model of Intermediate Complexity (EMIC), *Crucifix and Loutre* [2002] simulated a slight and rather monotonous decrease (5%) of the THC from 126 to 115 ka B.P. mainly in response to the increasing winter insolation. *Khodri et al.* [2003] simulated an increase of about 0.8 Sv (3.8%) from 125 to 115 ka B.P. using the CLIMBER 2 model. A larger increase by 8 Sv (20%) of THC between 120 and 116 ka B.P. is reported by *Wang and Mysak* [2002] using the McGill Paleoclimate Model. The relatively large increase in the latter study is related to the freshwater loss during ice sheet buildup which is not represented in this study. In contrast to most other studies the weakening THC in the early Eemian in our study is mainly due to the increased SSTs. Despite an increased poleward atmospheric moisture transport salinity even increases in the North Atlantic due to the advection of more saline waters from the tropics.

4.2. Comparison With Proxy Studies

[48] The simulated circulation changes in the Pacific, namely the intensification in the deep North and east Pacific and the weakening at intermediate levels are less prominent than those in the Atlantic but there is corroborating evidence from $\delta^{13}C$ records from the NACM [*Stott et al.*, 2000]. For the LIG, these records were interpreted to indicate a reduced ventilation for water masses shallower than 2 km and increased ventilation in the deep layers. In agreement with this, *Stott et al.* [2000] inferred also reduced oxygen concentrations close to anoxia in intermediate waters along the NACM. Our simulation predicts likewise, albeit only moderately reduced oxygen concentrations north of 30°N (<10%). This is linked to the reduced intermediate water production in the central North Pacific. However, owing to its coarse resolution, the ocean model simulates rather the open ocean signal. The topography does not resolve the small-scale basins with reduced connection to the open ocean. In these basins that parallel the NACM, however, even moderate changes in the intermediate open ocean ventilation as simulated in this study will probably have a pronounced impact which may have led locally to anoxic conditions as proposed by *Stott et al.* [2000].

4.2.1. Atmospheric and Vegetation Changes

[49] The simulated intensification of the Northern Hemisphere monsoon system (Figure 4e) is in excellent agreement with proxy data. In particular, the greening of the western part of Sahara desert during the Eemian is supported by reconstructions from pollen records [*van Andel and Tzedakis*, 1996]. However, also over SE Asia more humid conditions are inferred from oxygen isotope records from the South China Sea [*Jun et al.*, 2004].

[50] Likewise, the modeled northward expansion of boreal forests in the northern Hemisphere is well documented by pollen spectra and macrofossil assemblages from Alaska [*Edwards et al.*, 2003] and central Siberia where the tree line was located 800 km farther north [*Grichuk*, 1984].

4.2.2. Sea Surface Temperatures and Salinity

[51] *Cortijo et al.* [1999] have reconstructed strongest SST and sea surface salinity (SSS) increases in the northern North Atlantic (52–72°N) and only moderate warming and slightly increased SSS south of 40°N during the warm Eemian when ice volume was at its minimum. Hence, while the spatial SST pattern is in excellent agreement with the simulation (Figure 4a), modeled SSS are rather higher in the southern North Atlantic. A possible explanation for this discrepancy might be the beginning ice accumulation stimulated by decreasing summer insolation. This draws freshwater from the North Atlantic and stores it on land which is not accounted for in the model as ice sheets are kept fixed.

[52] A similar discrepancy is seen in the temporal evolution of SSTs. *Bauch and Kandiano* [2007] recently reconstructed the SST during the LIG for the North Atlantic and found a maximum warming between 125 and 121 ka B.P., which is clearly after the insolation maximum and even about 2000 a after the modeled warm optimum (127–125 ka B.P., Figure 2). Also here, the influence of extreme cold meltwaters from the penultimate deglaciation may have been dominant for long time and significantly influenced the SST in the North Atlantic directly and/or via a weaker THC. Thus the model result would probably agree better with the reconstructions when using an interactive dynamic ice sheet model.

4.2.3. Export Production and Nutrient Cycling

[53] The simulated strong increase in carbon export in the Barents and Kara seas (Figure 4d) is supported by benthic foraminiferal records [*Wollenburg et al.*, 2001] and by Dinoflagellate cysts [*Matthiessen and Knies*, 2001] indicating likewise warmer conditions there.

[54] The simulated increase in the tropical and subtropical Atlantic export production is supported by reconstructions of *Rühlemann et al.* [1996], who found production maxima in the western equatorial Atlantic during all warm substages of marine isotope stage 5. In contrast to our results however, most studies indicate diminished production in the eastern tropical and subtropical Atlantic [e.g., *Verardo and McIntyre*, 1994] during the early warm Eemian. This may be due to reduced iron fertilization originating from the drier areas in West Africa (triggered by more humid conditions during the warm period) which is not included in our model. However, the expanding vegetation coverage due to strengthened monsoon intensity in our simulations would certainly reduce the dust export offshore which then would feed back negatively on the production especially in the east Atlantic.

[55] Less and ambiguous data exist for the east equatorial Pacific carbon export which shows the strongest decline in our study. Most studies investigated glacial-interglacial

cycles with higher productivity [*Loubere et al.*, 2004] or rather slightly reduced productivity [*Lyle et al.*, 2002] during warm periods.

4.2.4. Carbonate Preservation and Atmospheric pCO$_2$

[56] The modeled increase in carbonate dissolution during the early warm Eemian is supported by multiproxy preservation records the North Atlantic that indicate increased corrosion with up to 45% loss of foraminiferal carbonate during interglacials [*Helmke and Bauch*, 2002]. Besides this, the simulation provides some implications for the interpretation of carbonate preservation proxies in the North Atlantic Ocean. In numerous studies such deep sea records have been interpreted as a proxy for varying presence of NADW versus AABW [e.g., *Henrich*, 1998; *Barker et al.*, 2004] with better preservation indicating strengthened NADW presence. Our results predict, however, despite an increase of roughly 20% in the North Atlantic overturning circulation from the warm optimum to 115 ka B.P. a significant decrease in preservation resulting in an decrease of roughly 10% of Atlantic carbonate budget (Figure 8a). This is explained by the uptake of oceanic CO_2 from the terrestrial biosphere which makes the ocean more acidic. Thus, during times of substantial changes in the terrestrial biosphere the use of preservation proxies for deep ventilation might be biased in the North Atlantic by reorganizations in the ocean-atmosphere-land carbon budget. A rough estimation of a possible bias is given below.

[57] *Barker et al.* [2004] have applied the calibration of planktonic foraminifera shell weight loss versus the pressure-normalized bottom water [$CO_3^=$] introduced by *Broecker and Clarc* [2003] on sites in the North Atlantic. They estimated an increase of 24 μmol/kg at around 4 km depth from the Last Glacial Maximum (LGM) to the Holocene (9.5 ka B.P.) which was interpreted to indicate the retreat of corrosive southern ocean water from the North Atlantic.

[58] We calculated *Broecker and Clarc*'s [2003] pressure normalized [$CO_3^=$] from our results and found a decrease from the warm optimum (with maximum carbon stored in the terrestrial biosphere) and 115 ka B.P. (representing the minimum) of up to 8 μmol/kg at around 4 km depth in the North Atlantic. In our model the major reason for this is the increasing CO_2 concentration in the bottom water which decreases the [$CO_3^=$]. Hence, if the increase in terrestrial carbon storage from the LGM to the Holocene (9.5 ka B.P.) is at similar magnitude as the change simulated for the LIG, this would mean that about one third of the LGM to Holocene increase in [$CO_3^=$] found by *Barker et al.* [2004] could be explained by the loss of CO_2 to the atmosphere and the increasing land biosphere storage. However, uncertainties in this estimate are associated with the state of deep convection in the North Atlantic which may have been suppressed during the LGM thus preventing an equilibrium of the atmospheric pCO$_2$ with carbonate sediments (carbonate compensation). On the other hand, the increase in terrestrial carbon storage from the LGM to the Holocene may have been 2 or 3 times the simulated changes presented in our study [*Joos et al.*, 2004]. However, our results provide a first estimate for the impact of changes in the carbon cycle on the North Atlantic carbonate preservation. This calls the commonly assumed simple relation-ship between carbonate preservation and deep water circulation at least for interglacials into question.

4.3. Atmospheric pCO$_2$

[59] During the warm period the simulated atmospheric pCO$_2$ is in good agreement with the Vostok record but with a tendency toward too high values after 120 ka B.P. (Figure 8b). Despite the large perturbations of the carbon cycle arising from the terrestrial biosphere (308 Gt carbon release) the model shows the ability to keep the pCO$_2$ within a narrow limit, which appears necessary to minimize the negative feedback of carbon release on the glacial inception. The carbonate sediment buffer in the North Atlantic is the dominant mechanism in this respect. A secondary mechanism arises from the cooling sea surface temperatures of $1-2$ K which can decrease the atmospheric pCO$_2$ by $10-20$ ppm [*Archer et al.*, 2004].

[60] Because of several limitations, the model fails, however, to simulate the steep pCO$_2$ decrease at the transition to the following glacial. The model does not account for the removal or addition of carbon by changes in limnic and paralic peatlands which might be an important factor with respect to the atmospheric pCO$_2$. *Gajewski et al.* [2001] have reconstructed a substantial expansion of boreal peatlands in North America and Asia during the warming of the Holocene. To store more carbon in the deep ocean calls for a stronger insulation of the deep ocean from the surface/atmosphere which is not seen in this study. Furthermore, additional important processes that are actually not represented in the model such as interactive dynamic ice sheets, allowing for supralysoclinal carbonate dissolution [*Milliman et al.*, 1999], and interactive ocean topography in combination with a better representation of continental shelves which governs the deposition of carbonate either in shallow coastal regions (essentially for coral reef buildup) or the deep sea may need to be involved in future studies.

5. Conclusions

[61] During the Eemian warm period at 126 ka B.P. changes in the atmospheric moisture transports result in a freshwater loss of the Atlantic catchment area north of 30°S by 34,000 m^3/s compared to a cooler period at the end of the Eemian (115 ka B.P.). However, contemporaneous surface water warming of up to 2 K lead to a weakening of the North Atlantic Overturning Circulation by up to 20%.

[62] In the North Pacific, warmer and fresher sea surface waters increase the stratification in the upper 2 km. This weakens the large-scale upwelling of deep waters in the North Pacific and results in a nutrient accumulation in the deeper layers and a corresponding depletion at the surface. In turn, this leads to strong reductions in productivity in areas with moderate or intense upwelling (e.g., equatorial east Pacific).

[63] The strong decrease in terrestrial carbon storage (308 Gt) taking place in the course of the Eemian due to climate cooling is nearly compensated by a corresponding uptake of the ocean. About one third of this uptake is balanced by the sedimentary carbonate buffer. The North Atlantic plays a key role in this respect as it interconnects the atmospheric carbon pool with the deep ocean and sediment pool. The

uptake of CO_2 corresponds to a shallowing of the lysocline in the North Atlantic by about 300 m.

References

Archer, D., P. Martin, B. Buffett, V. Brovkin, S. Rahmstorf, and A. Ganopolski (2004), The importance of ocean temperature to global biogeochemistry, *Earth Planet. Sci. Lett.*, *222*(2), 333–348.

Barker, S., T. Kiefer, and H. Elderfield (2004), Temporal changes in North Atlantic circulation constrained by planktonic foraminiferal shell weights, *Paleoceanography*, *19*, PA3008, doi:10.1029/2004PA001004.

Bauch, H. A., and E. S. Kandiano (2007), Evidence for early warming and cooling in North Atlantic surface waters during the last interglacial, *Paleoceanography*, *22*, PA1201, doi:10.1029/2005PA001252.

Berger, A. (1978), Long-term variation of daily insolation and quaternary climate change, *Atmos. Sci.*, *35*, 2362–2367.

Broecker, W. S., and E. Clarc (2003), Glacial age deep sea carbonate concentrations, *Geochem. Geophys. Geosyst.*, *4*(6), 1047, doi:10.1029/2003GC000506.

Brovkin, V., J. Bendtsen, M. Claussen, A. Ganopolski, C. Kubatzki, V. Petoukhov, and A. Andreev (2002), Carbon cycle, vegetation, and climate dynamics in the Holocene: Experiments with the CLIMBER-2 model, *Global Biogeochem. Cycles*, *16*(4), 1139, doi:10.1029/2001GB001662.

CAPE Last Interglacial Project Members (2006), Last Interglacial Arctic warmth confirms polar amplification of climate change, *Quat. Sci. Rev.*, *25*, 1383–1400.

Cortijo, E., S. Lehman, L. Keigwin, M. Chapman, D. Paillard, and L. Labeyrie (1999), Changes in meridional temperature and salinity gradients in the North Atlantic Ocean (30–72°N) during the last interglacial period, *Paleoceanography*, *14*(1), 23–33.

Crucifix, M., and M. F. Loutre (2002), Transient simulations over the last interglacial period (126–115 kyr BP): Feedback and forcing analysis, *Clim. Dyn.*, *19*, 417–433.

Edwards, M. E., T. D. Hamilton, S. A. Elias, N. H. Bigelow, and A. P. Krumhardt (2003), Interglacial extension of the boreal forest limit in the Noatak Valley, northwest Alaska: Evidence from an exhumed rivercut bluff and debris apron, *Arctic Antarct. Alpine Res.*, *35*, 460–468.

Gajewski, K., A. Viau, M. Sawada, D. Atkinson, and S. Wilson (2001), Sphagnum peatland distribution in North America and Eurasia during the past 21,000 years, *Global Biogeochem. Cycles*, *15*, 297–310.

Grichuk, V. P. (1984), Late Pleistocene vegetation history, in *Late Quaternary Environments of the Soviet Union*, edited by A. A. Velichko, pp. 155–178, Univ. of Minn. Press, Minneapolis.

Gröger, M., E. Maier-Reimer, U. Mikolajewicz, G. Schurgers, M. Vizcaíno, and A. Winguth (2007), Vegetation-climate feedbacks in transient simulations over the last interglacial (128,000–113,000 yr BP), in *The Climate of Past Interglacials*, edited by F. Sirocko et al., pp. 563–572, Elsevier, New York.

Helmke, J. P., and H. A. Bauch (2002), Glacial-interglacial carbonate preservation records in the Nordic Seas, *Global Planet. Change*, *33*(1–2), 15–28.

Henrich, R. (1998), Dynamics of Atlantic water advection to the Norwegian-Greenland Sea—A time-slice record of carbonate distribution in the last 300 ky, *Mar. Geol.*, *145*(1–2), 95–131.

Joos, F., S. Gerber, I. C. Prentice, B. L. Otto-Bliesner, and P. J. Valdes (2004), Transient simulations of Holocene atmospheric carbon dioxide and terrestrial carbon since the Last Glacial Maximum, *Global Biogeochem. Cycles*, *18*, GB2002, doi:10.1029/2003GB002156.

Jun, T., P. X. Wang, and X. R. Cheng (2004), Development of the East Asian monsoon and Northern Hemisphere glaciation: Oxygen isotope records from the South China Sea, *Quat. Sci. Rev.*, *23*(18–19), 2007–2016.

Kageyama, M., S. Charbit, C. Ritz, M. Khodri, and G. Ramstein (2004), Quantifying ice-sheet feedbacks during the last glacial inception, *Geophys. Res. Lett.*, *31*, L24203, doi:10.1029/2004GL021339.

Khodri, M., G. Ramstein, J. C. Duplessy, M. Kageyama, D. Paillard, and A. Ganopolski (2003), Modelling the climate evolution from the last interglacial to the start of the last glaciation: The role of Arctic Ocean freshwater budget, *Geophys. Res. Lett.*, *30*(12), 1606, doi:10.1029/2003GL017108.

Kubatzki, C., M. Montoya, S. Rahmstorf, A. Ganopolski, and M. Claussen (2000), Comparison of the last interglacial climate simulated by acoupled global model of intermediate complexity and an AOGCM, *Clim. Dyn.*, *16*, 799–814.

Kukla, G. J. (2000), The last interglacial, *Science*, *287*, 987–988, doi:10.1126/science.287.5455.987.

Loubere, P., F. Mekik, R. Francois, and S. Pichat (2004), Export fluxes of calcite in the eastern equatorial Pacific from the Last Glacial Maximum to present, *Paleoceanography*, *19*, PA2018, doi:10.1029/2003PA000986.

Lyle, M., A. Mix, and N. Pisias (2002), Export fluxes of calcite in the eastern equatorial Pacific from the Last Glacial Maximum to present, *Paleoceanography*, *17*(2), 1013, doi:10.1029/2000PA000538.

Maier–Reimer, E. (1993), Geochemical cycles in an ocean general circulation model. Preindustrial tracer distributions, *Global Biogeochem. Cycles*, *7*, 645–677.

Matthiessen, J., and J. Knies (2001), Dinoflagellate cyst evidence for warm interglacial conditions at the northern Barents Sea margin, during marine isotope stage 5, *J. Quat. Sci.*, *16*, 727–737.

Meissner, K. J., A. J. Weaver, H. D. Matthews, and P. M. Cox (2003), The role of land surface dynamics in glacial inception: A study with the UVic Earth system model, *Clim. Dyn.*, *21*, 515–537.

Mikolajewicz, U., M. Gröger, E. Maier–Reimer, G. Schurgers, M. Vizcaíno, and A. Winguth (2007), Long-term effects of anthropogenic CO_2 emissions simulated with a complex Earth system model, *Clim. Dyn.*, *28*(6), 599–633, doi:10.1007/s00382-006-0204-y.

Milliman, J. D., P. J. Troy, W. M. Balch, A. K. Adams, J. H. Li, and F. T. Mackenzie (1999), Biologically mediated dissolution of calcium carbonate above the chemical lysocline?, *Deep Sea Res., Part I*, *46*, 1653–1669.

Montoya, M., T. J. Crowley, and H. von Storch (1998), Temperatures at the last interglacial simulated by a coupled ocean-atmosphere climate model, *Paleoceanography*, *13*(2), 170–177.

Montoya, M., H. von Storch, and T. J. Crowley (2000), Climate simulation for 125 kyr BP with a coupled ocean-atmosphere general circulation model, *J. Clim.*, *13*, 1057–1071.

Petit, J. R., et al. (1999), Climate and atmospheric history of the past 420,000 years from the Vostok ice core, Antarctica, *Nature*, *399*, 429–436.

Roeckner, E., et al. (1992), Simulation of present-day climate with the ECHAM model: Impact of the model physics and resolution, *Rep. 93*, Max Planck Inst. for Meteorol., Hamburg.

Rühlemann, C., M. Frank, W. Hale, A. Mangini, S. Mulitza, P. J. Müller, and G. Wefer (1996), Late Quaternary productivity changes in the western equatorial Atlantic: Evidence from ^{230}TH-normalized carbonate and organic carbon accumulation rates, *Mar. Geol.*, *136*, 127–152.

Schurgers, G., U. Mikolajewicz, M. Gröger, E. Maier-Reimer, M. Vizcaíno, and A. Winguth (2006), Dynamics of the terrestrial biosphere, climate and atmospheric CO_2 concentration during interglacials: A comparison between Eemian and Holocene and Holocene, *Clim. Past*, *2*, 205–220.

Schurgers, G., U. Mikolajewicz, M. Gröger, E. Maier-Reimer, M. Vizcaíno, and A. Winguth (2007), The effect of land surface changes on Eemian climate, *Clim. Dyn.*, *29*, 357–373, doi:10.1007/s00382-007-0237-x.

Sitch, S., et al. (2003), Evaluation of ecosystem dynamics, plant geography and terrestrial carbon cycling in the LPJ dynamic global vegetation model, *Global Change Biol.*, *9*, 161–185.

Stott, L. D., M. Neumann, and D. Hammond (2000), Intermediate water ventilation on the northeastern Pacific margin inferred from benthic foraminiferal δ^{13}C, *Paleoceanography*, *15*(2), 161–169.

Takahashi, T., J. Olafsson, J. G. Goddard, D. W. Chipman, and S. C. Sutherland (1993), Seasonal variation of CO2 and nutrients in the high latitude surface oceans—A comparative study, *Global Biogeochem. cycles*, *7*, 843–878.

Tarasov, P., W. Granoszewski, E. Bezrukova, S. Brewer, M. Nita, A. Abzaeva, and H. Oberhänsli (2005), Quantitative reconstruction of the last interglacial vegetation and climate based on the pollen record from Lake Baikal, Russia, *Clim. Dyn.*, *25*, 625–637.

van Andel, T. H., and P. C. Tzedakis (1996), Paleolithic landscapes of Europe and environ-

ments: 150,000–25,000 years ago: An over-view, *Quat. Sci. Rev.*, *15*, 481–500.

Verardo, D. J., and A. McIntyre (1994), Production and destruction: Control of biogenous sedimentation in the tropical Atlantic 0–300,000 years B.P., *Paleoceanography*, *9*(1), 63–86.

Voss, R., and R. Sausen (1996), Techniques for asynchronous and periodically synchronous coupling of atmosphere and ocean models 2. Impact of variability, *Clim. Dyn.*, *12*, 605–614.

Wang, Z., and L. A. Mysak (2002), Simulation of the last glacial inception and rapid ice sheet growth in the McGill paleoclimate model, *Geophys. Res. Lett.*, *28*(23), 2102, doi:10.1029/2002GL015120.

Wollenburg, J., W. Kuhnt, and A. Mackensen (2001), Changes in Arctic Ocean paleoproductivity and hydrography during the last 145 ka: The benthic foraminiferal record, *Paleoceanography*, *16*(1), 65–77.

————————————

M. Gröger, Mainz Academy of Sciences, Humanities, and Literature, c/o IFM-GEOMAR, Kiel, Germany Wischhofstr. 1-3, D-24148 Kiel, Germany. (mgroeger@ifm-geomar.de)

E. Maier-Reimer and U. Mikolajewicz, Department of Ocean in the Earthsystem, Max Planck Institute for Meteorology, Bunderstrasse 53, D-21046 Hamburg, Germany.

G. Schurgers, Department for Physical Geography and Ecosystems Analysis, Lund University, Sölvegatan 12 223 62 Lund, Sweden.

M. Vizcaíno, Department of Geography, University of California, 531 McCone Hall, Berkeley, CA 94720-4740, USA.

A. Winguth, Department of Earth and Environmental Sciences, University of Texas at Arlington, Arlington, TX 76019-0049, USA.